Proceedings of ASME FEDSM'00
ASME 2000 Fluids Engineering Division Summer Meeting
Boston, Massachusetts, June 11-15, 2000

FEDSM2000-11196

HIGH SHEAR STRESS DETECTION WITH MICRO IMAGING CHIP AND DISCRETE WAVELETS TRANSFORM

Motoaki KIMURA, Masahiro TAKEI, Norimasa MIYAGI
Department of Mechanical Engineering
College of Science and Technology, Nihon Univ.
Tokyo, Japan
kimura@mech.cst.nihon-u.ac.jp

Chih-Ming HO
Mechanical and Aerospace Engineering Department
University of California, Los Angeles
Los Angeles, California, USA

Yoshifuru SAITO
Department of Electrical & Electronic Engineering
College of Technology, Hosei University
Tokyo Japan

Kiyoshi HORII
Shirayuri College
Tokyo Japan

Keywords: Turbulent Flow, Boundary Layer, MEMS, Shear Stress Sensor, Discrete Wavelets Transform

ABSTRACT

Shear stress stripe structure on the wall in turbulent boundary layer has been clearly visualized and found out by a combination of a shear stress sensor using MEMS (Micro-Electro-Mechanical-Systems) and discrete wavelets transform. The MEMS shear stress micro chip is designed and fabricated by surface micro-machining technology, contributing to obtaining the time-space two dimensional shear stress data. The discrete wavelets transform is a software technique to decompose the frequency level with the time and space information of the wave form. In details, the structure in lower Reynolds number is shown clearly on lower frequency wavelets level, the structure in high Reynolds number is done clearly on higher frequency wavelets level. To improve the detection result of the high shear stress area, the frequency levels are recomposed using the multiresolution filtering effect of wavelets transform. The experiments for the shear stress distribution were carried out on Re = 8700 and 17400.

INTRODUCTION

The presence of near-wall shear stress streaks in turbulent boundary layer has been observed for many years in flow visualization and experimental investigation [Cantwell 1891, Kline, et al. 1967, Kim, H. T., et al. 1971, Falco 1980, Head and Bandyopadhyay 1981, Smith and Metzler 1983]. At high Reynolds numbers, these streaks are typically very small in size and cannot be properly resolved by traditional measuring techniques. Numerical simulations indicate that the streaks are associated with stream-wise vortices in the viscous sub-layer. The rotational motion of these vortices imposes high fluctuating surface shear stress on the wall [Kim, J., et al. 1987]. There have been many measurement techniques for measuring shear stress. The hot-film technique and its variants have been widely used for the detailed investigations of fluctuating wall shear stress [Alfredsson, et al. 1988, Bruun 1995]. The direction sensitive laser Doppler anemometer is a candidate, which enables to evaluate both magnitude and direction of the wall shear stress. An optical method proposed by Naquwi is supposed to be capable of measuring the wall shear stress with high spatial resolution [Naquwi and Reynolds 1991]. No matter the instrument, the requirements of fine spatial resolution, fast frequency response, high sensitivity and convenience need to be satisfied for turbulent boundary layer research.

Recently, the availability of a new manufacturing process, micro-electro-mechanical-systems (MEMS) technology, has offered the possibility of sensing and controlling the small near-wall streaks [Ho, et al. 1997]. A multidisciplinary research collaboration between UCLA and Caltech has undergone to design and fabricate a large-scale distributed control system with integrated micromachined transducers and microelectronic circuits for surface shear stress control in turbulent boundary layers [Tung, et al. 1995, Ho and Tai 1996].

However, the distribution of stripe structure with MEMS is the integral value that is composed of various kinds of frequency ingredients. It leads to make the stripe structure ambiguous. Therefore, new techniques such as statistics analysis and frequency analysis to the image data are necessary for analyzing the structure in details. The stripe structure obtained with the micro imaging chip is clearly visualized with the statistics method [Kimura, et al. 1997]. Currently, wavelets transform has been started using for time-space frequency analysis instead of Fourier transform in mechanical engineering fields. The merits of the wavelets analysis is to be able to analyze the frequency not to erase the time-space information. Wavelets transform [Moret, et al. 1989] is roughly classified with two types, which are continuous wavelets transform and discrete wavelets transform. The discrete wavelets transform has been mainly used for picture image processing. The analysis enables to decompose and to compose picture image data quantitatively because of the orthonormal transform. Saito applied this idea to analyzing electromagnetic wave[Saito 1996].

The originality of this paper lies in applying discrete wavelets transform to visualizing and finding out the high shear stress region on the wall obtained with micro shear stress imaging chip. In this study, the stripe structure of shear stress in a turbulence boundary layer is extracted on various frequency levels with discrete wavelets transform. To visualize the high shear stress area more clearly, the frequency levels are recomposed using the multiresolution filtering effect of wavelets transform.

THEORY OF DISCRETE WAVELETS TRANSFORM

The wavelets transform matrix **S** that indicates wavelets spectrum is expressed by

$$\mathbf{S} = \mathbf{W} \cdot \mathbf{X} \tag{1}$$

Where, **W** is analyzing wavelets matrix and **X** is one dimensional input data matrix. The basic concept of the discrete wavelets transform is generalized by using fourth Daubechies function. The analyzing wavelets matrix is also an orthonormal function. The analyzing wavelets matrix **W** is acquired by a cascade algorithm on the basis of a function matrix **C**. The matrix **C** is shown in Eq.(2),

$$\mathbf{C} = \begin{pmatrix} c_0 & c_1 & c_2 & c_3 & 0 & 0 & \cdots & 0 & 0 & c_0 = \frac{1+\sqrt{3}}{4\sqrt{2}} \\ c_3 & -c_2 & c_1 & -c_0 & 0 & 0 & \cdots & 0 & 0 & c_1 = \frac{3+\sqrt{3}}{4\sqrt{2}} \\ 0 & 0 & c_0 & c_1 & c_2 & c_3 & \cdots & 0 & 0 & c_2 = \frac{3-\sqrt{3}}{4\sqrt{2}} \\ 0 & 0 & c_3 & -c_2 & c_1 & -c_0 & \cdots & 0 & 0 & c_3 = \frac{1-\sqrt{3}}{4\sqrt{2}} \\ \vdots & & & & & & & & & \\ 0 & 0 & 0 & 0 & 0 & 0 & \cdots & c_0 & c_1 & \\ 0 & 0 & 0 & 0 & 0 & 0 & \cdots & c_3 & -c_2 & \\ c_2 & c_3 & 0 & 0 & 0 & 0 & \cdots & 0 & 0 & \\ c_1 & -c_0 & 0 & 0 & 0 & 0 & \cdots & 0 & 0 & \end{pmatrix} \tag{2}$$

$$c_3 - c_2 + c_1 - c_0 = 0 \tag{3}$$

$$0\,c_3 - 1\,c_2 + 2\,c_1 - 3\,c_0 = 0 \tag{4}$$

Where, $\mathbf{C}^T \cdot \mathbf{C} = \mathbf{I}$. **I** is a unit matrix and $\mathbf{C}^T$ is a transpose matrix of **C**. The first line in Eq.(2) is called scaling coefficients and second line is called wavelets coefficients. Forth Daubechies function has four coefficients in a line. The first line shows a transform to obtain a sum value with weights of c_0, c_1, c_2 and c_3 on the input data. The second line shows a transform to obtain a difference value with weights of c_0, c_1, c_2 and c_3 on the input data. The third line shows a transform to translate the first line by two steps. The fourth line is a transform to do the second line by two steps. Eqs.(3) and (4) show the transformed values are zero when the input data are constant or are simply increased. To explain easily the process to acquire the analyzing wavelets matrix **W** from **C**, the matrix **X** is assumed to be one dimensional 16 elements,

$$\mathbf{X} = [x_1\, x_2\, x_3\, x_4\, x_5\, x_6\, x_7\, x_8\, x_9\, x_{10}\, x_{11}\, x_{12}\, x_{13}\, x_{14}\, x_{15}\, x_{16}]^T \tag{5}$$

From Eqs. (2) and (5), the transformed matrix **X'** is

$$\mathbf{X}' = \mathbf{C}_{16}\mathbf{X} = [s_1\, d_1\, s_2\, d_2\, s_3\, d_3\, s_4\, d_4\, s_5\, d_5\, s_6\, d_6\, s_7\, d_7\, s_8\, d_8]^T \tag{6}$$

Where, $\mathbf{C}_{16}$ is 16X16 matrix of **C**. The element s indicates the mean value and the element d indicates the difference value. The elements in the matrix **X'** are replaced by a matrix $\mathbf{P}_{16}$.

$$\mathbf{P}_{16}\mathbf{X}' = \mathbf{P}_{16}\,\mathbf{C}_{16}\mathbf{X} = [s_1\, s_2\, s_3\, s_4\, s_5\, s_6\, s_7\, s_8\, d_1\, d_2\, d_3\, d_4\, d_5\, d_6\, d_7\, d_8]^T \tag{7}$$

Where, $\mathbf{P}_{16}$ is defined as

$$\mathbf{P}_{16} = \begin{pmatrix} 1&0&0&0&0&0&0&0&0&0&0&0&0&0&0&0 \\ 0&0&1&0&0&0&0&0&0&0&0&0&0&0&0&0 \\ 0&0&0&0&1&0&0&0&0&0&0&0&0&0&0&0 \\ 0&0&0&0&0&0&1&0&0&0&0&0&0&0&0&0 \\ 0&0&0&0&0&0&0&0&1&0&0&0&0&0&0&0 \\ 0&0&0&0&0&0&0&0&0&0&1&0&0&0&0&0 \\ 0&0&0&0&0&0&0&0&0&0&0&0&1&0&0&0 \\ 0&0&0&0&0&0&0&0&0&0&0&0&0&0&1&0 \\ 0&1&0&0&0&0&0&0&0&0&0&0&0&0&0&0 \\ 0&0&0&1&0&0&0&0&0&0&0&0&0&0&0&0 \\ 0&0&0&0&0&1&0&0&0&0&0&0&0&0&0&0 \\ 0&0&0&0&0&0&0&1&0&0&0&0&0&0&0&0 \\ 0&0&0&0&0&0&0&0&0&1&0&0&0&0&0&0 \\ 0&0&0&0&0&0&0&0&0&0&0&1&0&0&0&0 \\ 0&0&0&0&0&0&0&0&0&0&0&0&0&1&0&0 \\ 0&0&0&0&0&0&0&0&0&0&0&0&0&0&0&1 \end{pmatrix} \tag{8}$$

Moreover, from Eq.(7), the transform is continuously carried out by **C** and **P** without any operations to the difference values,

$$\mathbf{W}^{(2)}\mathbf{X} = [S_1\, S_2\, S_3\, S_4\, D_1\, D_2\, D_3\, D_4\, d_1\, d_2\, d_3\, d_4\, d_5\, d_6\, d_7\, d_8]^T \tag{9}$$

$$\mathbf{S} = \mathbf{W}^{(3)}\mathbf{X} = [S_1\, S_2\, D_1\, D_2\, D_1\, D_2\, D_3\, D_4\, d_1\, d_2\, d_3\, d_4\, d_5\, d_6\, d_7\, d_8]^T \tag{10}$$

Where,

$$\mathbf{W}^{(2)} = (\mathbf{P}_{16}\mathbf{C}'_{16})(\mathbf{P}_{16}\mathbf{C}_{16}) \tag{11}$$

$$W^{(3)} = (P_{16}'' C_{16}'')(P_{16}' C_{16}')(P_{16}C_{16}) \quad (12)$$

$$P_{16}' = \begin{bmatrix} P_8 & 0 \\ 0 & I_8 \end{bmatrix} C_{16}' = \begin{bmatrix} C_8 & 0 \\ 0 & I_8 \end{bmatrix} P_{16}'' = \begin{bmatrix} P_4 & 0 \\ 0 & I_{12} \end{bmatrix} C_{16}'' = \begin{bmatrix} C_4 & 0 \\ 0 & I_{12} \end{bmatrix} \quad (13)$$

$W^{(3)}$ is a analyzing wavelets matrix that is W in Eq.(1). The wavelets spectrum S in Eq.(1) is $W^{(3)}X$ in Eq.(10). In Eq.(9), S_1 indicates the mean value from s_1 to s_4 in Eq.(7). S_2 indicates the mean value from s_3 to s_6 that translate by two steps. D_1 indicates the difference value from s_1 to s_4. In Eq.(10), S_1 indicates the mean value from S_1 to S_4 in Eq.(9). D_1 indicates the difference value from S_1 to S_4 in Eq.(9). From Eq.(10), the input data are transformed to the mean values and the difference values with valuable resolution levels by the discrete wavelets transform. The input data are divided into a range from high frequency to low frequency. From Eq.(10), the inverse wavelets transform is,

$$X = [W^{(3)}]^T S \quad (14)$$

$$[W^{(3)}]^T = [(P_{16}''C_{16}'')(P_{16}'C_{16}')(P_{16}C_{16})]^T$$
$$= C_{16}^T P_{16}^T (C_{16}')^T (P_{16}')^T (C_{16}'')^T (P_{16}'')^T \quad (15)$$

From Eq.(14), the multiresolution is,

$$X = [W^{(3)}]^T S = [W^{(3)}]^T S_0 + [W^{(3)}]^T S_1 + [W^{(3)}]^T S_2 + [W^{(3)}]^T S_3 \quad (16)$$

Where,

$$S_0 = [S_1\ S_2\ 0\ 0\ 0\ 0\ 0\ 0\ 0\ 0\ 0\ 0\ 0\ 0\ 0\ 0]^T$$
$$S_1 = [0\ 0\ D_1\ D_2\ 0\ 0\ 0\ 0\ 0\ 0\ 0\ 0\ 0\ 0\ 0\ 0]^T$$
$$S_2 = [0\ 0\ 0\ 0\ D_1\ D_2\ D_3\ D_4\ 0\ 0\ 0\ 0\ 0\ 0\ 0\ 0]^T$$
$$S_3 = [0\ 0\ 0\ 0\ 0\ 0\ 0\ 0\ d_1\ d_2\ d_3\ d_4\ d_5\ d_6\ d_7\ d_8]^T \quad (17)$$

In the case of sixteen input data and fourth Daubechies, multiresolution indicates from Level 0 to Level 3.
The two dimensional wavelets spectrum S is obtained from

$$S = W_n \cdot X \cdot W_m^T \quad (18)$$

Where, W_m^T is a transpose matrix of W_m. From Eq.(18), the discrete inverse wavelets transform is expressed by

$$X = W_n^T \cdot S \cdot W_m \quad (19)$$

In general, in the case that input data is 2^n and Daubechies function is kth, the final wavelets spectrum is obtained after the wavelets transform in Eq.(15) continues until the number of final summation elements is less than k.
In this study, 16th Daubechies function is used instead of the fourth Daubechies function that is explained the above as analyzing wavelets. The fundamental properties are similar to fourth Daubechies function. In the case that 16th Daubechies function and the space data number 32 (all space 9.6mm; pseudo-space are included) and the time data number 512 (all measurement time 51.2ms), the wavelets level of the multiresolution is decomposed from level 0 to level 6 in the time, and from level 0 to level 3 in the space.

EXPERIMENTS

Micro Shear Stress Imaging Chip

A micro shear-stress imaging chip, which is composed of multiple micro shear-stress sensors [Jiang, et al. 1996], is exhibited in Fig.1. On the imaging chip are five rows of micro sensors, three of which contain an array of 25 sensors. The other two rows contain 5 sensors each. Within each array, the distance from each sensor to the next one is 300 μm. The sensors are thermal type. Figure 2 shows top and cross-section of a micro shear stress sensor. Each micro sensor consists of a

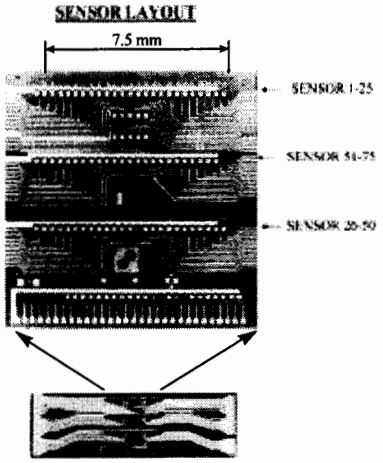

Fig. 1 A surface shear stress imaging chip

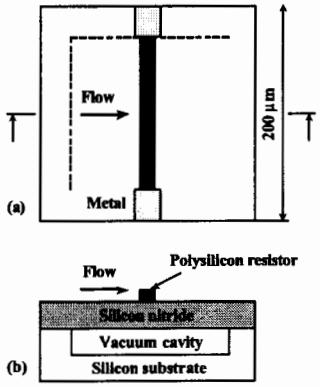

Fig. 2 Schematic top (a) and cross-sectional (b) views of the micro shear stress sensor

150 μm long, 3 μm wide, and 0.45 μm thick polysilicon resistor wire and a 1.2 μm thick, 200 x 200 μm^2 silicon nitride diaphragm that seals off a 2 μm deep vacuum cavity underneath. The purpose of the cavity is to reduce heat transfer from the resistor wire to the substrate and increase the sensitivity of the sensor [Huang, et al. 1996]. The sensors are connected to external constant temperature mode circuits, similar to a hot-wire anemometer, through gold bonding wires and driven at an overheat ratio of 1.1. Output from the anemometer circuits is digitized by a 64-channel Keithly Metrabyte ADC board in a Pentium 120 based PC. At a gain of 10, the sensitivity of the shear stress sensor is about 1 V/Pa with a frequency response of 25 kHz.

Shear Stress Sensor Calibration and Temperature Compensation

The heating power of a shear stress sensor operating in steady state can be correlated with wall shear stress τ as follows [Bruun 1995]:

$$i^2 R^2 = (T_f - T)(A + B\tau^{1/3}) \quad (20)$$

Where T_f and T are the temperature of the heated sensor and the measured fluid, respectively, R is the resistance of the sensor, i is the heating current going through the sensor, and A and B are calibration constants. In order to correlate the output voltage with the wall shear stress: τ, two theoretical methods are used here. In the first method, τ in a fully developed turbulent flow of the channel is related to the stream-wise pressure gradient by:

$$dP_x / dx = -\tau / h \quad (21)$$

Where P_x is the local pressure, x is the stream-wise coordinate, and h is the half height of the wind channel. The pressure drop and output voltage of the sensor was measured at different center velocities of the channel ranging from 8 m/s to 20 m/s. If the temperature of the measured fluid T is constant, the wall shear stress can be directly related to the output voltage Eo by a sixth-order polynomial with the data:

$$\tau = a_0 + a_1 E_0 + ... + a_6 E_0^6 \quad (22)$$

Where, a_0 a_1, a_2 ....a_6 are calibration constants. These constants were calibrated in the channel flow in a downstream region where the turbulent flow was fully developed. In the second method, an empirical relationship between the Reynolds number and the wall shear stress in a fully developed channel flow is obtained [Hussain and Reynolds 1970], by using:

$$u_\tau / u_\infty = 0.1079 Re^{-0.089} \quad (23)$$
$$\tau = u_\tau^2 \rho \quad (24)$$

Where u_τ is the friction velocity, u_∞ is the center velocity of the channel, Re is calculated using the mean centerline velocity, and ρ is the air density. We first measure the stream-wise pressure gradient and calculate τ by using Eq.(21). Afterwards, we use the second method give by Eqs.(23) and (24) to calculate the wall shear stress again. Good agreement is found between shear-stress values calculated by using both methods.

When the ambient fluid temperature, T, varies during the measurement, a thermal correction should be applied. To find out the correction coefficient of the temperature compensation, previous micro shear stress sensor vs. fine thermocouple simultaneous measurements have done in the channel flow at 10 m/s under the room temperature range (19.0 °C to 22.0 °C). The slope of the sensor output as a function of temperature is -310 mV/°C. Temperature compensation was achieved by collecting both ambient temperature and shear stress data first then correcting accordingly with software after experiment.

Experimental Setup

The study was carried out in a turbulent channel flow facility as Fig.3(a). The channel, constructed of 13 mm Plexiglas, is 610 mm x 25.4 mm in cross-section and 4880 mm long. An axial blower controlled by a DC power supply generates the air flow in the channel. Previous hot-wire measurement indicates that the channel flow, at a centerline velocity of 10 m/s, consists of a laminar entrance flow and a fully developed turbulent flow in the downstream half of the channel. The micro shear stress imaging chip was packaged into a specially designed PC board as shown in Fig.3(b) and flush mounted to the wall at 4267 mm from the inlet of the channel, where a fully developed turbulent channel flow exists for the velocity range tested. One array of 25 micro shear-stress sensors that covers a distance of 7.5 mm is used to measure the instantaneous spanwise distribution of the turbulent surface shear stress. The experiment was carried out at different *Re's* ($=hu_\infty/\nu$, where h=half width of the channel, u_∞ =centerline velocity) ranging from 8,758 to 17,517.

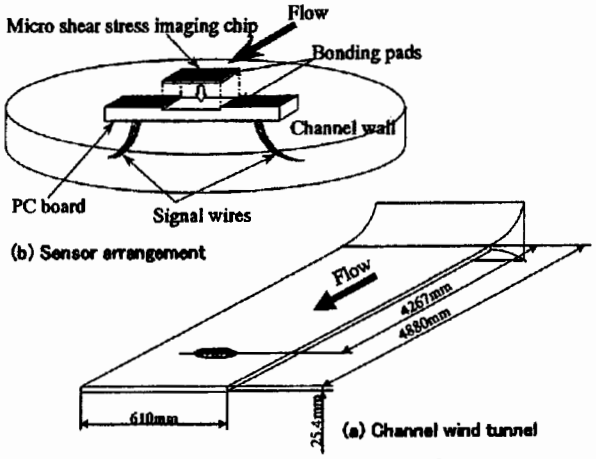

Fig. 3 Sensor arrangement and wind tunnel

Shear-Stress Distribution

Fig.4 shows the contour of 2-D shear stress distributions measured by the 25 sensors covering an area 7.5 mm in wide, 100 ms in time for two different Re numbers. The shear stress values are normalized with the minimum value 0.0 and the maximum value 1.0 on each Re number. Areas of high shear stress are marked by light-gray while dark-gray represents low shear stress. Note that the transverse scale of the longitudinal high shear-stress streaks varies with Re numbers. The streaks are narrower and packed more densely as Re number increases. They also appear at the shorter time interval as Re number increase.

ANALYSIS AND DISCUSSION

Analysis Method

The multiresolution analysis is carried out to the wavelets spectrum by the inverse wavelets transform in Eq.(25), after the wavelets transform in Eq.(18) is operated to 25 X 512 shear stress distribution data in Fig.4 to obtain the wavelets spectrums. Zero is put into the matrix position from 26 to 32 in x coordinate in Fig.3 intentionally because the data number of discrete wavelets transform is subject to nth power of two. In the case of sixteenth Daubechies function and 512 ($=2^9$) input data, the multiresolution classifies to seven levels as shown in Eq.(19).

$$
\begin{aligned}
X &= [W_n{}^{(5)}]^T \cdot S \cdot [W_m{}^{(5)}] \\
&= [W_n{}^{(5)}]^T \cdot S_0 \cdot [W_m{}^{(5)}] + [W_n{}^{(5)}]^T \cdot S_1 \cdot [W_m{}^{(5)}] \\
&\quad + [W_n{}^{(5)}]^T \cdot S_2 \cdot [W_m{}^{(5)}] + [W_n{}^{(5)}]^T \cdot S_3 \cdot [W_m{}^{(5)}] \\
&\quad + [W_n{}^{(5)}]^T \cdot S_4 \cdot [W_m{}^{(5)}] + [W_n{}^{(5)}]^T \cdot S_5 \cdot [W_m{}^{(5)}] \\
&\quad + [W_n{}^{(5)}]^T \cdot S_6 \cdot [W_m{}^{(5)}]
\end{aligned}
\qquad \text{—(25)}
$$

$W^{(5)}$ indicates the five times operation to obtain Daubechies matrix from a matrix C in Eq.(2).

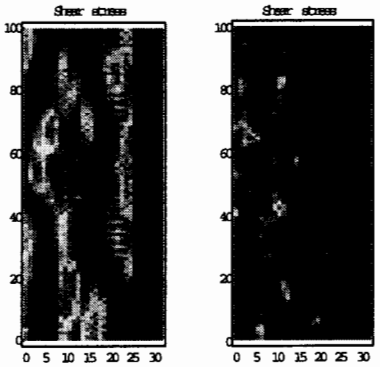

(a) Re=8700 (b)Re=17400

x-direction [X 300 μ m], y-direction [X 0.1ms]

Fig. 4 Shear stress measured with the imaging chip

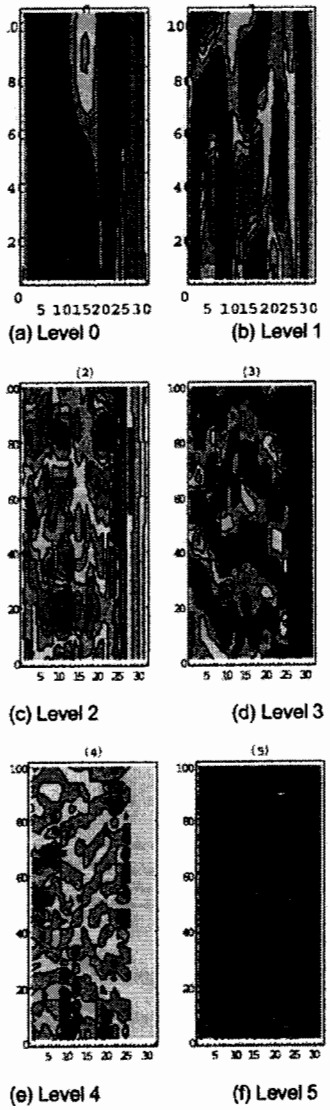

(a) Level 0 (b) Level 1

(c) Level 2 (d) Level 3

(e) Level 4 (f) Level 5

Fig. 5 Multiresolution analysis in Re=8700

Analysis Results & Discussion

Figs.5 and 6 show the multiresolution with contours in the low Re number and the high Re number, respectively. The high shear stress shows it with black, the low shear stress shows it with white. Level 6 is not shown because the noise seems to be dominant. The patterns adding all levels from Level 0 to Level 6 recover completely the original shear stress distributions in Fig.4, because Daubechies analyzing wavelets are orthonormal functions. From these figures, the original input

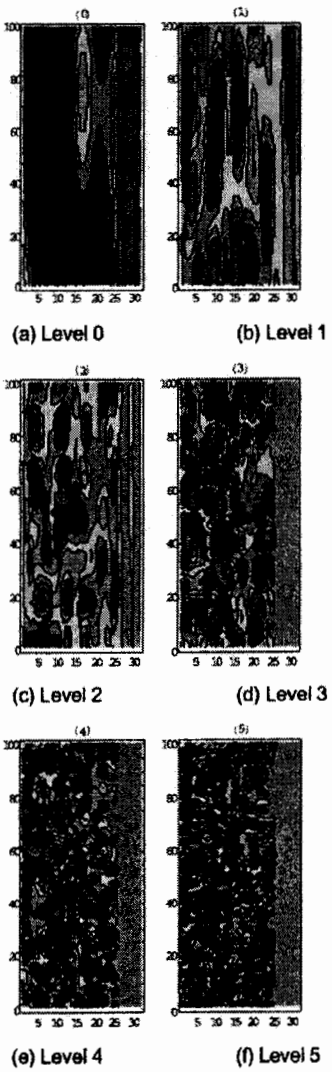

(a) Level 0 (b) Level 1

(c) Level 2 (d) Level 3

(e) Level 4 (f) Level 5

Fig. 6 Multiresolution analysis in Re=17400

data are decomposed from a low frequency component Level 0 to a high frequency component Level 5. The each level operator a kind of band pass filter. The shear stress stripe structures on the wall due to a series of bursting events in the low speed shear stress area are visualized clearly on each frequency level without erasing the time and space information.

Our effort is directed to qualifying the characteristics of mean-wall streaks and providing control guideline for controlling the skin friction on the wall. To improve the predicting procedure of high shear stress areas on the wall, the discrete wavelets transform is applied to the shear stress area

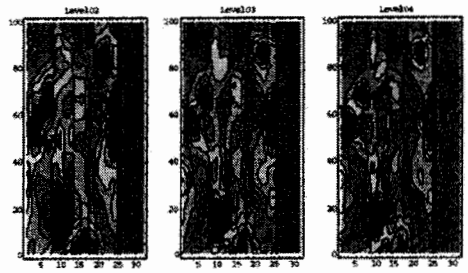

Fig. 7 Multiresolution filtering in Re=8700

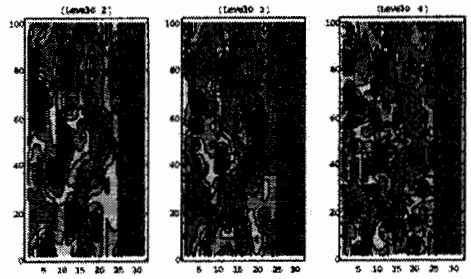

Fig. 8 Multiresolution filtering in Re=17400

filtering. The micro shear stress imager can measure the high shear stress area, which is created by the induced stream-wise eddy due to the bursting events near the wall. There are several ms order wave due to the passing bursting event and the higher order wave due to the eddy dissipation order or noise in the data. The higher order waves disturb the identification of the high shear stress area.

The discrete wavelets transform is applied in order to suppress the higher order waves and discriminate more clearly the high shear stress area. Figures 7 and 8 show the recomposed contours with the multiresolution results in the high and low Re numbers. Level 02 indicates Level 0 + Level 1 + Level 2, and so on. In terms of the low Re number, Re = 8700, it seems that the black areas in the contours from Level 02 to Level 04 indicate more clearly the high shear stress areas. This is the filtering effect appears due to the suppression on the high levels, Level 5 and Level 6. In the case of Re = 17400, Level 04 contour indicates the high shear stress more clearly than the normal contour, Fig.4. Further the complex area shape of high shear stress due to high Re number is simplified from level 04 to level 02 by the filtering procedure. It is considered that the higher frequency range is suppressed by the filtering effect of the multiresolution and recomposed procedure. The filtering technique is very important to find out easily and correctly the high shear stress area from the background fluctuation of shear stress on the wall.

Figure 9 indicate the time trace of the original data (data) and the filtered data (0to3, 0to4 and 0to5) at the point where the maximum shear stress appears. It is almost same the original data and the filtered data with 0to5 over. The high frequency range is suppressed by the filtering effect. In the case of 0to1 or 0to2, high order filtering, it is need to take care of the time delay from the original data. One of the aims of studying the 2-D shear-stress distribution is to develop an identification criterion that can be used by control logic circuit to detect the passage of the high shear-stress streaks. To develop such a criterion, the characteristics of the streaks, lengths, peak shear-stress levels and shear-stress slopes are examined.

Peak, length and slope of high shear stress streaks are illustrated in Fig.10. To evaluate the shear stress the non-dimensionalized shear stress τ^* is defined as:

$$\tau^* = (\tau - \tau_m) / \tau' \qquad (26)$$

Where τ_m is the time-average shear stress and τ' is the rms of shear stress. The peak is defined as the maximum shear stress in the streak. The length is defined as the streak length in time of limit above $\tau^* = 0.3$. The threshold $\tau^* = 0.3$ is decided by the area separation of high shear stress streaks to pick up high shear stress streaks, and the background fluctuation level of shear stress as mentioned in section high shear stress streaks [Kimura, et al. 1999]. The slope is defined as the front-end (30% of the streak length in time under the original data) shear-stress gradient of the streak. It is to be desired that the time is as short as possible to predict the peak in early stage. The 30% of the streak length in time is determined based on the convergence of the correlation coefficient to be discussed in the following sections.

To identify a possible relationship between the peak shear-stress and shear-stress slope of the streaks, their correlation coefficient are computed. The correlation coefficient is computed based on about 200 streaks obtained at fixed Re number. Figure 11 shows the variation of the correlation coefficient for the original data and filtered data. In the case of the original data the correlation coefficient change from 0.45 to 0.1 as Re increase. In the case of the filtered data, 0to3 and 0to4, the correlation coefficients between slope and peak are around 0.5. This result indicates that discrete wavelets transform using the multiresolution and recompose filtering is effective method to improve the detection result of high shear stress region on a wall skin friction.

Conclusions

A micro machine shear-stress imaging chip was used to measure the instantaneous shear-stress distribution in a turbulent wall boundary layer on conditions from Reynolds number 8700 to 17400. The two dimensional shear stress distributions are visualized and filtered with discrete wavelets transform. As a result, the following becomes clear.

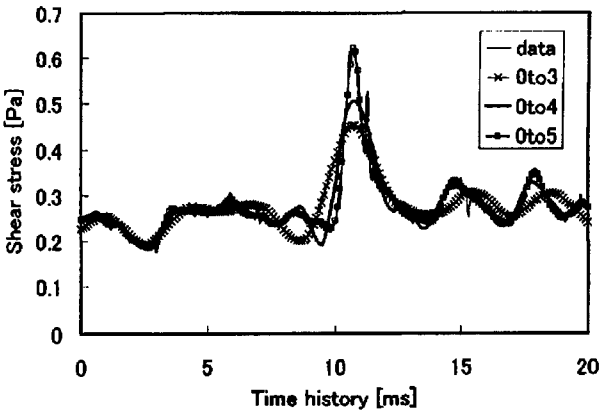

Fig. 9 Sample data

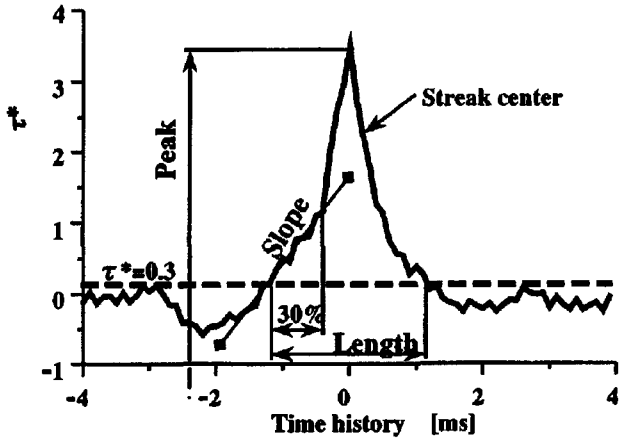

Fig. 10 Peak, Length and Slope of streaks

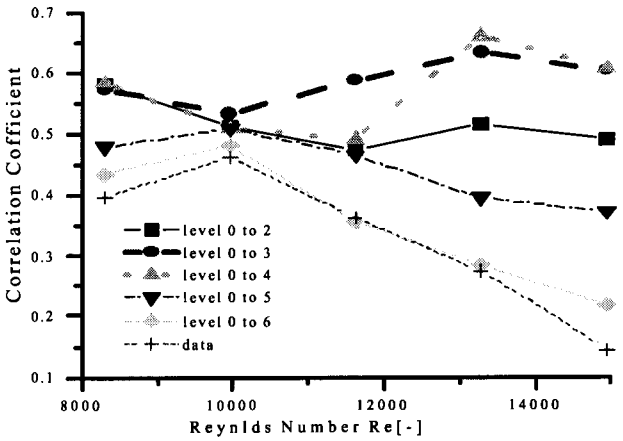

Fig. 11 Correlation coefficient between peak shear-stress and front slope of the high shear-stress area

(1) The structure of wall shear stress are able to be decomposed and be clearly visualized on each level without erasing time-space information.

(2) The high shear stress areas are identified more clearly by discrete wavelets transform using the multiresolution and recompose filtering effect. The filtering effect offers the possibility of predicting the high shear stress area on the wall. This result will be implemented into the algorithm for the integrated turbulent boundary layer control system.

ACKNOWLEDGMENTS

A special promotive research fund from Nihon University, college of science and technology and also, an URI project from US Air Force Office of Scientific Research support this work. The authors wish to thank Dr. Y.-C. Tai from the California Institute of Technology for the use of the micro shear stress image chip.

REFERENCES

Alfredsson, P. H., Johansson, A. V., Haritonidis, J. H. and Eckelmann, H., (1988), "The Fluctuating Wall-Shear Stress and the Velocity Field in the Viscous Sublayer", *Phys. Fluids*, 31 (5), pp.1026-1033.

Bruun, H. H., (1995), "Hot-Wire Anemometry," Oxford University Press, pp.272-286.

Cantwell, B. J., (1981), "Organized Motion in Turbulent Flow," *Ann.Rev.Fluid Mech.*, Vol. 13, pp.457-515.

Falco, R., (1980), "The Production of Turbulence Near a Wall," *AIAA Paper*, 80-1356.

Head, M. R. and Bandyopadhyay, P., (1981), "New Aspects of Turbulent Boundary-Layer Structure," *J. Fluid Mech.* Vol.107, pp.297-338.

Ho, C. M., Tung, S. and Tai, Y. C., (1996), "Interactive Control of Wall Structures by MEMS-Based Transducers," *Advances in Turbulence, Proceedings of the Sixth European Turbulence Conference*, pp.413, Lausanne, Switzerland, July.

Ho, C. M., Tung, S, Lee, G. B., Tai, Y. C., Jiang, F. and Tsao, T., (1997), "MEMS-A Technology for Advancements in Aerospace Engineering," *AIAA Paper* 97-0545.

Huang, J. B., Tung, S., Ho, C. H., Liu, C. and Tai, Y. C., (1996), "Improved Micro Thermal Shear-Stress Sensor," *IEEE Transactions on Instrumentation and Measurement*, Vol.45, No.2, pp.570.

Hussain, A. K. M. F. and Reynolds, W. C., (1970) "The Mechanics of a Perturbation Wave in Turbulent Shear Stress Flow," *Air Force Office of Scientific Report* 70-1655TR.

Jiang, F., Tai, Y. C., Gupta, B., Goodman, R., Tung, S., Huang, J. B. and Ho, C. M., (1996), "A Surface-Micromachined Shear Stress Imager," *Proceedings of the 9th International IEEE Workshop on MEMS*, p.110, San Diego.

Kim, H. T., Kline, S. J. and Reynolds, W. C., (1971), "The Production of Turbulence Near a Smooth Wall in a Turbulent Boundary Layer," *J. Fluid Mech.* Vol.50, Part1, pp.133-160.

Kim, J., Moin, P. and Moser, R., (1987), "Turbulent Statistics in Fully Developed Channel Flow at Low Reynolds Number," *J. Fluid Mech.* Vol.177, pp.133-166.

Kimura, M., Tung, S., Lew, J., Ho, C. M., Jiang, F., Tai, Y. C., (1997) "MEMS for Aerodynamic Control", *28th AIAA Fluid Dynamics Conference, AIAA Paper*, 97-2118

Kimura, M., Tung, S., Lew, J., Ho, C. M., Jiang, F., Tai, Y. C., (1999) "Measurements of Wall Shear Stress of a Turbulent Boundary Layer using a Micro-Shear-Stress Imaging Chip," *Fluid Dynamics Research*, Vol.24, pp.329-342

Kline, S. J., Reynolds, W. C., Schraub, F. A., Runstadler, P. W., (1967), "The Structure of Turbulent Boundary Layer," *J. Fluid Mech.* Vol.30, No.4, pp.741-773.

Molet, F. et al., (1989), "Wavelets Propagation and Sampling Theory", *Geophysics*, Vol.11

Naqwi, A. A. and Reynolds, W. C., (1991), "Measurement of Turbulent Wall Velocity Gradients using Cylindrical Waves of Laser Light," *Experiments in Fluids*, Vol.10, pp.257-266.

Saito, Y., (1996), "Wavelets Analysis for Computational Electromagnetics, (in Japanese) ", *Trans. IEE of Japan*, Vol. 116A, No10, pp833-839

Smith, C. R. and Metzler, S.P., (1983), "The Characteristics of Low- Speed Streaks in the Near-Wall Region of a Turbulent Boundary Layer," *J.Fluid Mech.* Vol.129, pp.27-54.

Tung, S., Hong, H., Huang, J. B., Ho, C. M., Liu, C. and Tai, Y. C., (1995) "Control of a Streamwise Vortex by a Mechanical Actuator," *Proceedings of 10th Symposium on Turbulent Shear Flows*, Vol.1, pp.1-19, Pennsylvania, USA.